

ON THE ISOTROPY OF THE DYNAMIC MECHANICAL AND FAILURE PROPERTIES OF SWAGED TUNGSTEN HEAVY ALLOYS

D. Rittel¹, R. Levin and A. Dorogoy

Faculty of Mechanical Engineering
Technion, Israel Institute of Technology
32000 Haifa, Israel

ABSTRACT

The quasi-static and dynamic mechanical and failure properties of a swaged tungsten base heavy alloy rod have been investigated, with emphasis on the orientation of the specimens in the rod. Three orientations were considered, namely 0°, 45° and 90° with respect to the longitudinal axis of the rod. Compression, tension and dominant shear tests were carried out. With the exception of the 0° orientation, all the orientations displayed quite similar mechanical characteristics in tension and compression. Dynamic shear revealed a critical strain for adiabatic shear failure of $\epsilon_c \approx 0.13$, independent of the orientation, and quite inferior to the quasi-static ductility. The present study confirms previous results obtained for one (generally unspecified) orientation and extends them to three orientations. Failure mechanisms were thoroughly characterized and it appears that significant damage does not develop prior to final failure. It is concluded that, for practical purposes, the swaged heavy alloy considered here can be regarded as *isotropic* from a mechanical and failure point of view, in spite of its microstructural anisotropy resulting from the swaging process.

Keywords: tungsten, heavy alloy, isotropy, mechanical properties, failure

¹ Corresponding author: email: merittel@tx.technion.ac.il

I. INTRODUCTION

The class of alloys referred to as "heavy alloys" generally consists of the families of alloys where the primary elemental components have a high density, such as W, Ta, or U. Tungsten base heavy alloys are produced by liquid phase sintering of elemental powders, essentially W, Ni and Fe. The high density of these materials (typically in excess of 17 gr/cm³) makes these alloys suitable for armor piercing purposes (kinetic penetrators)^[1, 14]. The typical microstructure of a tungsten base heavy alloy consists of W (BCC) nearly spherical single crystals surrounded by a binding phase (FCC matrix) which is a solid solution of W, Ni and Fe. The mechanical properties of these alloys have been extensively studied, both quasi-statically (e.g.^[2-5]) and dynamically (e.g.^[6-12]), with emphasis, in the last decade, on their ability to undergo shear localization in the form of adiabatic shear banding^[8-11]. The heavy alloys can be produced in a variety of near-final shapes, but the most frequently encountered shape is that of cylindrical rods, that may be subjected to a series of thermomechanical treatments to improve their mechanical properties. For example, these alloys are frequently swaged to improve their strength. The various studies to date have dealt with several compositions and thermomechanical treatments. The experimental specimens used to characterize the mechanical behavior of this material all had characteristic dimensions comparable to those of the rod, with the exception of the specimens used for pressure-shear experiments^[11] that were thin disks, 50μm-200μm thick. The above-mentioned references show that heavy alloys are strain-rate sensitive. At low strain rates, the material exhibits some strain-hardening that gradually fades out when the strain rate increases ($\dot{\epsilon} \approx 10^3 \text{ s}^{-1}$), followed by strain softening at higher strain rates. Strain softening has been attributed to thermal softening, as a result of thermomechanical coupling^[5]. When the individual constituents or the composite are considered, it should first be noted that lack of strain hardening has been reported for dynamically loaded cold worked pure tungsten^[6]. In addition, dynamic strain softening of textured tungsten has also been reported for the <001> orientation^[13]. Zhou and Clifton^[11], who tested an alloy whose composition is representative of the binding matrix, did not observe high strain rate related softening effects. Back to the tungsten base heavy alloy, all the above mentioned references report a tendency for adiabatic shear failure at high strain rates, as modeled in the work of Zhou et al.^[10]. Ramesh^[9] reports a critical shear strain to failure of $\gamma_c = 0.08 - 0.13$, to be contrasted with the significantly higher values reported by Zhou and Clifton^[11] of $\gamma_c = 1 - 1.5$. Quite surprisingly, the mechanical investigations carried out so far on swaged rod materials (e.g.^[8, 9]) have not taken into account a *possible anisotropy of the mechanical properties*, as would be expected to result from the forming process. The issue of adiabatic shear band formation has not been related to material orientation, even if the ballistic efficiency of the material depends on its tendency to fail by this mechanism^[14]. A noticeable exception can be found in the work of Weisbrod and Rittel^[15] and

that of Rittel and Weisbrod ^[16], who studied the anisotropy of the quasi-static and dynamic fracture properties of a tungsten base heavy alloy. Yet, concerning the mechanical properties and propensity of tungsten base heavy alloys to undergo adiabatic shear failure, one would naturally expect that the material orientation be a determinant factor.

Consequently, a thorough investigation of this issue was carried out for a 90:7:3 weight percent tungsten/iron/nickel alloy that had been 25% swaged. Three selected orientations (0°, 45° and 90° with respect to the longitudinal axis) were tested statically and dynamically in tension and in compression. In addition, a newly developed specimen, the Shear Compression Specimen (SCS) was used to evaluate the response of the material to shear dominant deformation ^[17-19]. This paper examines the influence of material anisotropy on the quasi-static and dynamic mechanical properties of the investigated alloy.

The paper is organized as follows: section 1 introduces the material, experimental specimens and procedures, detailing the Shear Compression Specimen (SCS). Section 2 starts with selected basic numerical results about the SCS, followed by the various mechanical characteristics measured. Section 3 describes the specific failure micromechanisms of the investigated alloy. Section 4 summarizes and discusses the main results of this work, while Section 5 brings the concluding remarks.

II. EXPERIMENTAL

II.1 Material

The material investigated in this work is a tungsten-iron-nickel alloy, of weight ratio 90:7:3. The material was liquid-phase sintered as a cylindrical rod. It was heat treated using proprietary treatments, and subsequently 25% swaged to a final diameter of 26 mm. The specimens were subsequently machined from the rod and supplied for the present study.

II.2 Specimens

The experimental specimens were machined in three selected orientations: 0°, 45° and 90° with respect to the longitudinal axis of the original rod. The specimens, their dimensions and denomination are shown in Fig. 1. As shown in this figure, the specimens were essentially machined from the central part of the rod. Compression specimens are basically cylindrical specimens, whereas the tensile specimens are short, threaded specimens. A total of 14 and 6 specimens per orientation were tested in compression and tension respectively. The small size of the specimens is dictated by the final diameter of the rod. Parallelepiped Shear Compression Specimens ^[17-19] were machined with their 45° slot oriented along each of the above-mentioned directions. Three slot (gauge) widths per orientation were selected: 2.5 mm, 1mm and 0.25 mm. 5 specimens of each gauge width were tested per orientation.

The notch root radius was 0.2mm for the wider gauges and of the order of 0.1 mm for the 0.25 mm gauge.

II.3 Testing

Static compression and tension tests were performed on a servo-hydraulic, computer controlled MTS 810 machine under displacement control. Tensile specimens were instrumented with a clip-on extensometer. Compression tests were carried out by inserting the cylinder between two hard steel flat platens lubricated with petroleum jelly. The same procedure was applied to quasi-static testing of the SCS. In all the cases, the machine compliance was determined prior to testing, to improve the accuracy of the stress-strain diagrams.

Dynamic testing was carried out on a Split Hopkinson Pressure Bar (Kolsky apparatus ^[20]). The diameter of the bars was 12.7 mm, and they were made of a similar tungsten base heavy alloy. Geometric dispersion of the measured signals was accounted for and corrected using Lifshitz and Leber's algorithm ^[21]. Both cylindrical and SCS specimens were tested with this setup. Dynamic tension was performed on a modified Kolsky tension bar, 12.7 mm diameter, made of 17-4 PH steel. Here too, dispersion corrections were applied to the signals.

Characterization of the failure mechanisms was achieved firstly through SEM fractographic analysis. In addition, longitudinal sections were prepared by sectioning Ni plated fracture surfaces at mid-thickness of the gauge. Such longitudinal sections allow assessment of the nature and extent of the damaged zone below the main fracture surface, all along the crack path.

III. RESULTS

III.1 Numerical modeling of the SCS ^[23]

Previous work with the SCS ^[17-19, 23] has shown that the (Von Mises) equivalent stress, $\hat{\sigma}_{eqv}$, and strain, $\hat{\epsilon}_{eqv}$, can be related to the applied load and specimen geometry by the following simple formulas:

$$\hat{\sigma}_{eqv} = k_1 \left(1 - k_2 \hat{\epsilon}_{eqv} \right) \frac{P}{Dt} \quad (1)$$

and

$$\hat{\epsilon}_{eqv} = k_3 \frac{d}{h} \quad ; \quad \dot{\hat{\epsilon}}_{eqv} = k_3 \frac{\dot{d}}{h} \quad (2)$$

where P is the applied load, d the prescribed displacement, D the specimen width, t is the thickness of the gauge, and $h=1.414w$ its height. The coefficients k_1 , k_2 , and k_3 must be determined numerically, and are generally observed to be dependent on both the material (via its hardening modulus) and the gauge height, h . A finite element model of the SCS was generated and solved using ANSYS finite-element package [22]. Bilinear material behavior was assumed and the elastic-plastic problem was solved, allowing for geometrical nonlinearities by using a large strain formulation. Young's and tangent moduli, as well as the yield strength of the various orientations, were determined from the tensile and compressive tests. Both $\hat{\sigma}_{eqv}$ and $\hat{\epsilon}_{eqv}$ were calculated by averaging the results on a mid-section of the specimen gauge. The boundary conditions consisted of a prescribed (negative) vertical displacement, while one node on the bottom face of the specimen was fully constrained. Determination of the k_i consisted of calculating the resultant load-displacement curve as a result of the prescribed displacement for a given material with assumed bilinear behavior. Earlier work showed that the calculated averaged $\hat{\sigma}_{eqv} - \hat{\epsilon}_{eqv}$ curve on a mid-section of the gauge accurately reproduced the assumed bilinear constitutive law [23]. $P - \hat{\epsilon}_{eqv}$ and $d - \hat{\epsilon}_{eqv}$ relations were thus identified using polynomial regressions, according to eqns. (1) and (2). A set of k_i was determined for each orientation and gauge width, as summarized in Table I. The analyses clearly showed that all three orientations could be characterized by similar coefficients k_i for a given gauge width.

As will be shown in the sequel, the validation of the overall approach, as shown in previous works [16-18] lies in the requirement that the equivalent stress-strain curve obtained using the SCS be similar to that obtained either through tension or compression tests, although the latter are limited in the range of strains attainable.

III.2 Quasi-static and dynamic compression

Typical quasi-static compression stress-strain curves are shown for the 3 orientations in Fig. 2. This figure shows that the material exhibits similar moderate strain-hardening in all orientations, and that the 0° orientation is weaker than the other two orientations. Typical dynamic stress-strain curves are shown in Fig. 3. Here too, the 0° orientation appears to be weaker. Comparing Figs. 2 and 3 shows the characteristic strain rate sensitivity [6-13] together with a noticeable decrease in strain hardening, turning the material into elastic-almost perfectly plastic at high rates.

III.2 Quasi-static and dynamic tension

As shown in Fig 4, the typical quasi-static tensile behavior is rather similar for all the orientations. The attainable range of strains is quite limited (about 0.03) as the specimens tend to neck early during

deformation. Up to this strain level, strain-hardening is moderate. Table II summarizes the various values of Young's modulus measured in the quasi-static tensile tests.

Fig. 5 shows characteristic dynamic stress-strain curves. All the tests reveal an similar initial inertial peak that stems from lack of equilibrium across the specimen (Fig. 5a for the 0° orientation.). Fig. 5b shows smoothed stress-strain curves for all three orientations together, without the inertial peak. This figure reveals similar characteristics, i.e. almost perfect plastic flow and similar strength levels. Once again, one may note the marked strain rate sensitivity of the material. Moreover, contrary to the compression tests, tension tests (static and dynamic) do not show a weaker orientation in this material.

III.3 Quasi-static and dynamic Shear Compression testing

A distinctive feature of the SCS is that the deformation of the gage is dominated by shear, even if this is not pure shear, as mentioned in the introduction. Moreover, because of its geometry, the gage section does not neck or barrel markedly so that large strains can develop without problems, over a variety of strain rates. Fig. 6 shows the typical $\hat{\sigma}_{eqv} - \hat{\epsilon}_{eqv}$ curves for the SC specimens, along with the curves obtained from tensile specimens. The high similarity between the two types of results validates the choice of the k_i coefficients. Here, large strains of the order of 0.35 and more are obtained, and the strain hardening capacity of the material is evident. One should emphasize that the specimens did not fracture at these strain levels as the test was interrupted arbitrarily. Therefore, a greater ductility can be expected for those tests shown in Fig. 6.

Eqns. (1) and (2) are also applicable to dynamic testing, and characteristic results are shown in Fig. 7. At high strain rates, the material shows again a lack of strain hardening and noticeable strain rate sensitivity, as expected. In addition, a certain degree of softening can be noted past $\epsilon = 0.1$ for those specimens whose testing ended by fracture, as shown in Fig. 7. We observed that all the failed specimens fractured at an overall strain of $\epsilon_c \approx 0.13$, as manifested by the unloading part of the stress-strain curve that does not unload parallel to the "elastic" part. It should be emphasized that the dynamic failure strain is considerably smaller than its quasi-static counterpart.

In these experiments, the yield stress could not be accurately determined using extensometric techniques. Consequently, we report values of the proportional stress which corresponds to the end of the proportional stress-strain domain. The proportional stress gives an estimate of the "macroscopic" yield stress of the material. Table III summarizes typical proportional stress data for each orientation and test.

III.3 Failure mechanisms

III.3.1 Tension tests

Fig. 8 (a-c) shows the failure micromechanisms of a quasi-static tensile specimen of each orientation.

For the 0° specimens, the fracture surface comprises essentially cleavage of the W grains with little evidence of ductile matrix failure. This is confirmed by observing the various profiles showing cleavage of the W grains and some matrix decohesion.

For the 45° specimens, one distinguishes cleavage, interfacial (binding necks) failure, and little matrix deformation. The profiles indicate the same mechanisms, but also reveal multiple cleavage cracks in a single W grain.

For the 90° specimens, the above failure mechanisms are complemented by evidence of ductile matrix failure (dimples). The profiles show that matrix failure occurs on the fracture surface only, as no damage is detected below it. Here too, multiple W grain cleavage is observed.

Fig. 9 (a-c) shows the failure micromechanisms of a dynamic tensile specimen of each orientation.

For the 0° specimens, the fracture surface comprises cleavage of the W grains and abundant ductile matrix failure. This is confirmed by observing the various profiles that also show that matrix damage remains confined to the fracture surface.

For the 45° specimens, one distinguishes essentially interfacial (binding necks) failure and noticeable matrix deformation. The profiles indicate the same mechanisms, but also reveal that the matrix damage now extends below the main fracture plane.

For the 90° specimens, one can note cleavage and interfacial failure, as well as profuse matrix failure (dimples). The profiles indicate the same mechanisms, but also reveal that significant matrix damage extends below the main fracture plane.

III.3.2 Shear dominant tests

Quasi-static dominant shear is characterized in Fig. 10 (a-c) for orientations 0°, 45° and 90° respectively.

Here, we examined specimens that *did not fracture* after various levels of strain ($\epsilon=0.3-0.45$). In all the cases, one can clearly see that the grains within the sheared gauge rotate considerably with respect to those grains outside the gage. Moreover, these grains elongate noticeably without apparent damage in the adjacent matrix. These observations indicate a large ductility of the material when shear deformation is considered. All 3 orientations show identical response in this respect.

Dynamic dominant shear is characterized in Fig 11 (a-c), for orientations 0° , 45° and 90° respectively. All specimens fractured, and we examined longitudinal mid-sections of the specimens, after having plated the fracture surface with Ni prior to sectioning.

All 3 orientations show an identical tendency to shear localization over a very small number of grains (typically less than 5 grains). This tendency is characterized by highly elongated tungsten grains that have undergone considerable deformation in the vicinity of the fracture surface. In this respect, all three directions respond identically in terms of shear localization under dynamic loading conditions, as was also noted from the mechanical characteristics. The interesting point is that we did not notice any significant damage, either at the tungsten-matrix interface or with the matrix itself, as this was the case in some orientations for different loading conditions.

The fracture surfaces of the dynamically fractured SCS's all show similar features, regardless of the orientation. Severe wearing of the tungsten grains is observed, which indicates a high level of frictional stresses. This is characteristic of shear failure mechanism, beyond which there is not much more to observe. A comparative summary of the failure micromechanisms is given in Table III (the reader is referred to ^[24] for additional information on the failure mechanisms).

IV. DISCUSSION

The static and dynamic mechanical properties of a swaged tungsten base heavy alloy have been systematically investigated, taking for the first time material orientation into account.

From a general point of view, the present results agree very well, and extend previous reports on the rate sensitivity of the material, and its lack of strain hardening during dynamic deformation. These points were all noted for compression and torsion tests by Ramesh and coworkers ^[8-9].

By contrast, the dynamic tensile behavior of these alloys has not been much investigated. Gero et al. ^[25] reported the operation of different failure mechanisms in quasi-static tension and compression. Specifically, these authors showed the role of the W-W interface in tension as opposed to the development of larger strains in both the matrix and the W grains in compression of the 0° orientation tested in the mentioned reference ^[26]. The present work does not address the failure mechanisms in compression, as the majority of the specimens did not fail during this test. However, the dynamic tensile failure mechanisms were observed to vary with the orientation of the specimen. This interesting observation complements partly Gero et al.'s ^[25] observations in the sense that failure mechanisms in compression might be orientation dependent, as they are in tension.

The SCS test allows for the development of large strains which are not usually attained with other tests. Due to the dominant state of shear, one can compare the results to those obtained using pure shear specimens ^[8] on the one hand. Yet, the concept of equivalent stress and strain also allows

comparison with other uniaxial tests on the other hand. Numerical calculations and experimental observations have shown that the deformation is homogeneous with the specimen gauge, as long as it does not become localized, as this is the case for (adiabatic) shear band formation ^[19, 23]. Having validated the numerical results pertaining to the data processing technique for the SCS, it is interesting to note that the static and dynamic shear response of the material yield results that are comparable to those obtained with the other two testing techniques. Beyond the mere comparison of yield stress, it should be noted that the high rate SCS tests show some strain softening similar to that reported by Kim et al.^[12] for their compression tests. Moreover, when comparing with the shear tests of Ramesh ^[9], our results show the very same trend for a dynamic failure strain that is noticeably smaller than its quasi-static counterpart. The present value of the failure strain $\epsilon_c \approx 0.13$, i.e. $\gamma_c \approx 0.225$. This value is slightly higher than that reported by Ramesh ^[9] of $\gamma_c \approx 0.08 - 0.13$, and the difference may be due to differences in material composition and thermal treatments. However, the failure strain is considerably smaller than the value reported by Zhou and Clifton^[11], and one can tentatively relate this discrepancy to the very small specimen size used by these authors. Indeed, a thickness of 50 μm -200 μm represents a small number of tungsten grains, so that a size effect may possibly influence the determination of the failure strain. Yet, one of the novelties of this work is that the observed value of the failure strain can now be extended to three main material orientations, thus showing an identical propensity to adiabatic shear failure in all three orientations. Therefore, to summarize the main results to that point, our results show that both the quasi-static and the dynamic mechanical properties of the investigated alloy are reasonably *isotropic*, thus generalizing previous observations. Moreover, the *failure characteristics*, mostly the dynamic ones, exhibit the same isotropy in terms of adiabatic shear band formation. These results are of prime importance when it comes to selecting an appropriate constitutive model and failure criterion for this material for numerical modeling purposes.

Yet, the very observation of an isotropic response for this swaged material contradicts all intuitive expectation. At this stage, one should discuss the deformation and failure mechanisms reported in this work. The failure mechanisms and their extent are distinct for each kind of test (static and dynamic) and orientation, to some extent. Comparing this observation with the observed isotropy of the mechanical response indicates that the failure mechanisms play no a significant role during most of the deformation process. In other words, the various damage mechanisms that are observed after fracture, such as multiple cleavage of the W grains or interfacial decohesion at the W-matrix interface, all occur most likely very close to the final failure strain. The material does not undergo a significant level of damage during its plastic flow until near final failure. This point is further confirmed, e.g. by the observations of the sheared, but un-fractured longitudinal sections of the SCS, that all show significant plastic flow in the gage section without any appreciable sign of damage, whatever the orientation is. These same sections show a very high ductility of the composite (tungsten grains *and* matrix) as a

whole regardless of the orientation. It is also interesting to note that the actual adiabatic shear failure zone is quite narrow (typically less than 5 W grains) and proceeds largely through a continuum of highly sheared W grains to a stage where the binding matrix is almost indiscernible. Again, the longitudinal sections through the fractured shear band do not reveal apparent signs of damage in the matrix or at the W-matrix or W-W interfaces, either. This shows again that the various failure mechanisms all operate during final fracture of the specimen rather than developing gradually throughout the deformation process.

It should be noted in passing that this observation stands at odds with the qualification of "brittle material" that is very often found in the literature when the tungsten component of heavy alloys is mentioned. These particles are far from being brittle, as can be seen in all the micrographs shown here. The confusion arises most likely from the fact that the tungsten particles in the present alloy (and its likes) are single crystals that can exhibit considerable plastic flow, as opposed to polycrystalline tungsten.

Finally, it seems that material anisotropy should induce mechanical anisotropy, for both the mechanical and failure properties of the investigated material. The results presented in this study point to an apparent lack of such anisotropy, which may be stated in another way. Namely, there is certainly some anisotropy of the mechanical and failure properties, however, the experimental "resolution" of the present tests, along with the natural dispersion of the experimental results, did not allow for its observation, meaning that for engineering purposes, the investigated material can be considered as mechanically isotropic. This observation indicates that the 25% diameter reduction due to the swaging process does not induce anisotropy of the mechanical properties close to the center of the rod.

V. CONCLUSIONS

The influence of material anisotropy of a swaged tungsten base heavy alloy on its mechanical and failure properties was examined for the first time, both quasi-statically and dynamically. Three orientations were tested in compression, tension and shear dominant tests: 0°, 45° and 90° with respect to the longitudinal axis of the swaged rod.

The main conclusions of the present study can be summarized as follows:

- The 0° orientation is weaker than the other two orientations in quasi-static and dynamic compression, in agreement with previous observations ^[25]. However, this difference is not observed for the other tests and all orientations exhibit quite similar mechanical properties.
- The investigated material is noticeably strain-rate sensitive in accordance with previous observations. At high strain rates, the strain hardening capacity vanishes, turning the material into elastic-almost ideally plastic. This result applies for all three orientations.

- The newly introduced SCS allows for development of large strains that are otherwise limited by mechanical instabilities. Quasi-static testing shows a high ductility for all three orientations where $\varepsilon > 0.35$.
- By contrast, all the failed SCS fracture at an equivalent strain of $\varepsilon_e \approx 0.13$. This value is of the same order of magnitude as that reported by Ramesh ^[9], and can, again, be generalized to all the orientations in question.
- Characteristic failure mechanisms have been identified for each test and orientation, using SEM metallographic and fractographic analysis.
- Little damage is identified below the main fracture plane. In all the tests and orientations, the material exhibits a high overall ductility for each of its components.
- A marked tendency for shear localization was observed for all the orientations, again with little damage. These observations indicate that the various damage and failure mechanisms all operate close to the final failure strain, rather than throughout the deformation process.
- Mechanical and failure anisotropy was not observed in the present work, possibly due to its small extent. This indicates the minor influence of the swaging process close to the rod's center.
- Therefore, for all practical purposes, the investigated swaged heavy alloy can be treated as mechanically isotropic.

Acknowledgements

Financial support was provided through grant # 030-052. The Fund for Promotion of Research at Technion is acknowledged for partial support. The authors thank Drs. R. Gero, L. Boruchin, A. Pikus and C. Weinberger for stimulating discussions.

REFERENCES

1. W.E. Gurwell, R.G. Nelson, G.B. Dudder and N.C. Davis, PNL Report #5218, Richland, WA.
2. R.H. Krock and L.A. Shepard: *Transactions TMS-AIME*, 1963, 227, pp. 1127-1134.
3. D. Rittel, I. Roman and M. Bercovier: *ASME Transactions, Journal of Engineering Materials and Technology*, 1986, 108, pp. 159-162.
4. D. Rittel and I. Roman: *Materials Science and Engineering*, 1986, 82, pp. 93-99.
5. R.G. O'Donnell and R.L. Woddward: *Met. Trans. A*, 1990, 21A, pp. 744-748.
6. A. K. Zurek and G.T. Gray III: *J. de Physique IV Coll. C3*, 1991, 1, pp. C3-631-C3-637.
7. H. Couque, J. Lankford and A. Bose: *J. Phys. III France*, 1992, 2, pp. 2225-2238.
8. K.T. Ramesh and R.S. Coates: *Met. Trans. A*, 1992, 23A, pp. 2625-2630.
9. K.T. Ramesh: *Mech. of Materials*, 1994, 17, pp. 165-173.
10. M. Zhou, A. Needleman and R.J. Clifton: *J. Mech. Phys. Solids*, 1994, 42(3), pp. 423-458.
11. M. Zhou and R.J. Clifton: *J. Applied Mechanics*, 1997, 64, pp. 487- 494.
12. D.S. Kim, S. Nemat-Nasser, J.B. Isaacs and D. Lischer: *Mech. of Materials*, 1998, 28, pp. 227-236.
13. G. Subhash, Y.J. Lee and G. Ravichandran: *Acta Metall. Mater.*, 1994, 42(1), pp. 319-330.
14. L.S. Magness Jr.: *Mech. of Materials*, 1994, 17, pp. 147-154.
15. G. Weisbrod and D. Rittel: *Intl. Journal of Fracture*, 2000, 104(1), pp. 91-104.
16. D. Rittel and G. Weisbrod: *Int. Journal of Fracture*, 2001, 212, pp. 87-98.
17. D. Rittel, S. Lee and G. Ravichandran: *Experimental Mechanics*, 2002, 42(1), pp. 58-64.
18. D. Rittel, S. Lee and G. Ravichandran: *Mech. of Materials*, 2002, 34, pp. 627-642.
19. M. Vural, D. Rittel and G. Ravichandran: *Metallurgical and Material Transactions A*, 2003, 34A (12), 2873-2885.
20. H. Kolsky: *P. Phys. Soc. Lond.*, 1949, 62-B, pp. 676-700.
21. J.M. Lifshitz and H. Leber: *Int. J. Impact Engng.*, 1994, 15(6), 723-733.
22. ANSYS, User's Manual: (2003), Ansys Inc.
23. A. Dorogoy and D. Rittel, *Int. J. Plasticity*, 2004, submitted.

24. R.G. O'Donnell and R.L. Woddward: *J. Matls. Sc.*, 2000, 35, pp. 4319-4324.
25. R. Gero, L. Borukhin and I. Pikus: *Matls. Sc. Engng.*, 2001, A302, pp. 162-167.
26. R. Gero, L. Borukhin and I. Pikus: *Private communication*, 2003.

TABLES

W	k_1	k_2	k_3
0.3 mm	0.861	0.152	0.213
1.0 mm	0.927	0.219	0.628
2.5 mm	0.955	0.276	0.931

Table I: Coefficients for the SCS

E	0°	45°	90°
[GPa]	≈347	≈ 350	≈ 361

Table II: Young's modulus – quasi-static tension

Proportional Limit [MPa]	0°	45°	90°
Quasi-static compression	≈ 1250	≈ 1500	≈ 1500
Dynamic compression	≈ 1750	≈ 2000	≈ 2000
Quasi-static tension	≈ 1450	≈ 1500	≈ 1500
Dynamic tension	≈ 2000	≈ 2000	≈ 2000
Quasi-static shear (SCS)	≈ 1500	≈ 1500	≈ 1500
Dynamic shear (SCS)	≈ 2000	≈ 2000	≈ 2000

Table III: Summary of characteristic proportional limits

ORIENTATION	STATIC TENSION	DYNAMIC TENSION	STATIC SHEAR	DYNAMIC SHEAR
0°	Cleavage-W	- Cleavage-W - <i>Superficial</i> matrix ductile failure	- Homogeneous deformation	- Localized shear - Essentially W grains - No matrix damage
45°	- Cleavage-W - Multiple cleavage - W-W failure	- W-W failure - <i>Extended</i> matrix ductile failure	- Homogeneous deformation	- Localized shear - Essentially W grains - No matrix damage
90°	- Cleavage-W - Multiple cleavage - W-W failure - Superficial matrix ductile failure	- Cleavage-W - W-W failure - <i>Extended</i> matrix ductile failure	- Homogeneous deformation	- Localized shear - Essentially W grains - No matrix damage

Table IV: Summary of the main failure mechanisms observed for the 3 orientations

FIGURE CAPTIONS

- Figure 1: Experimental specimens. (a) compression, (b) tension and (c) shear compression (SCS)
- Figure 2: Quasi-static compression. Typical true stress-strain curves for each orientation.
- Figure 3: Dynamic compression. Typical true stress-strain curves for each orientation.
- Figure 4: Quasi-static tension. Typical true stress-strain curves for each orientation.
- Figure 5: Dynamic tension. (a) Typical true stress-strain curves for 0° orientation. Note the initial inertial peak and the bilinear approximation. (b) Typical true stress-strain curves for each orientation.
- Figure 6: Quasi-static shear compression tests. True stress-strain curves obtained for each orientation from cylindrical specimens and from SCS's. Note the high similarity of the results while larger strains are attainable with the SCS.
- Figure 7: Dynamic shear compression tests. Typical true stress-strain curves for each orientation. The 90° specimen fractured, as evidenced from the unloading part of the graph.
- Figure 8: Failure mechanisms of quasi-static tensile specimens at (a) 0°, (b) 45° and (c) 90°. For each orientation, 2 longitudinal sections (perpendicular to the fracture plane) and one SEM fractograph are shown.
- Figure 9: Failure mechanisms of dynamic tensile specimens at (a) 0°, (b) 45° and (c) 90°.
- Figure10: Quasi-static SCS specimens. Longitudinal sections of deformed specimens that did not fracture, at (a) 0°- $\epsilon=0.45$, (b) 45° - $\epsilon=0.35$ and (c) 90°- $\epsilon=0.30$. Note the grains' rotation and elongation within the gauge section
- Figure11: Dynamic SCS specimens. Longitudinal sections of fractured specimens, perpendicular to the fracture surface, at (a) 0°, (b) 45° and (c) 90°. It can be noted that the individual grains in the immediate vicinity of the fracture surface are heavily elongated and sheared.

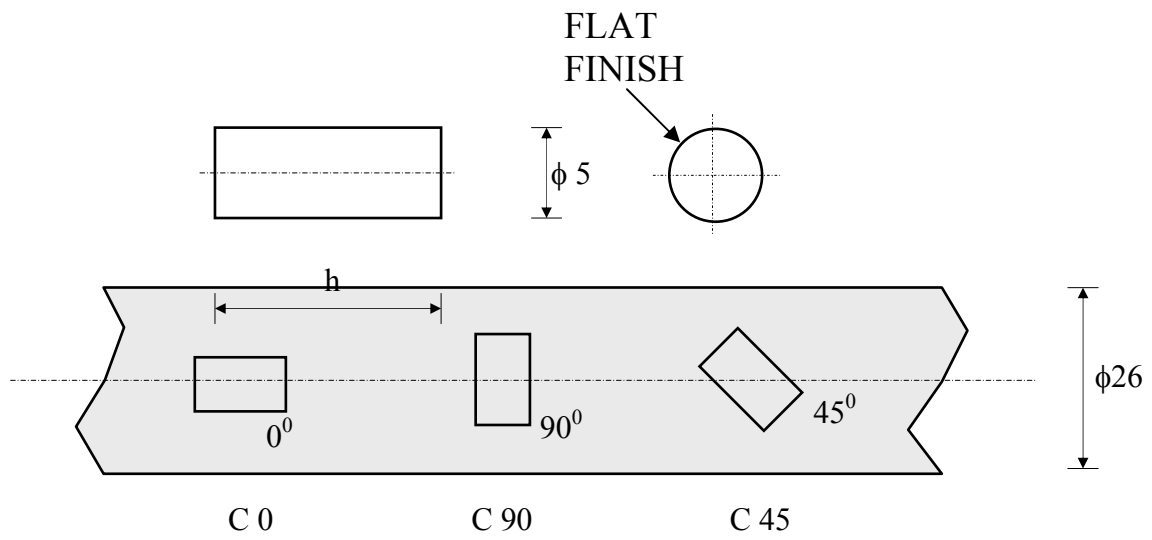


FIGURE 1A

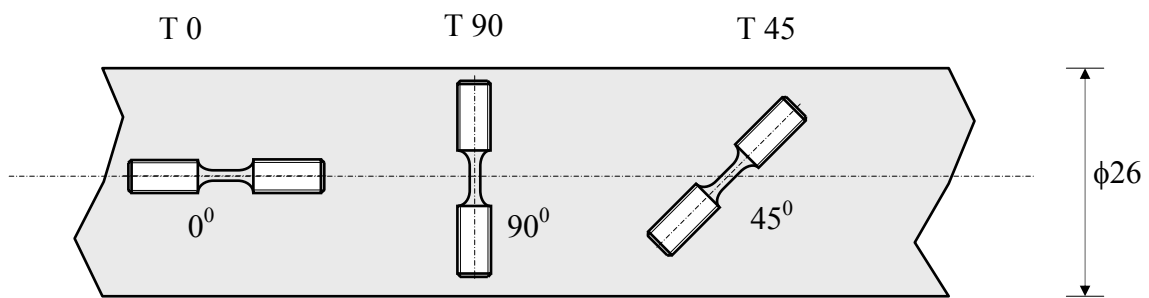


FIGURE 1B

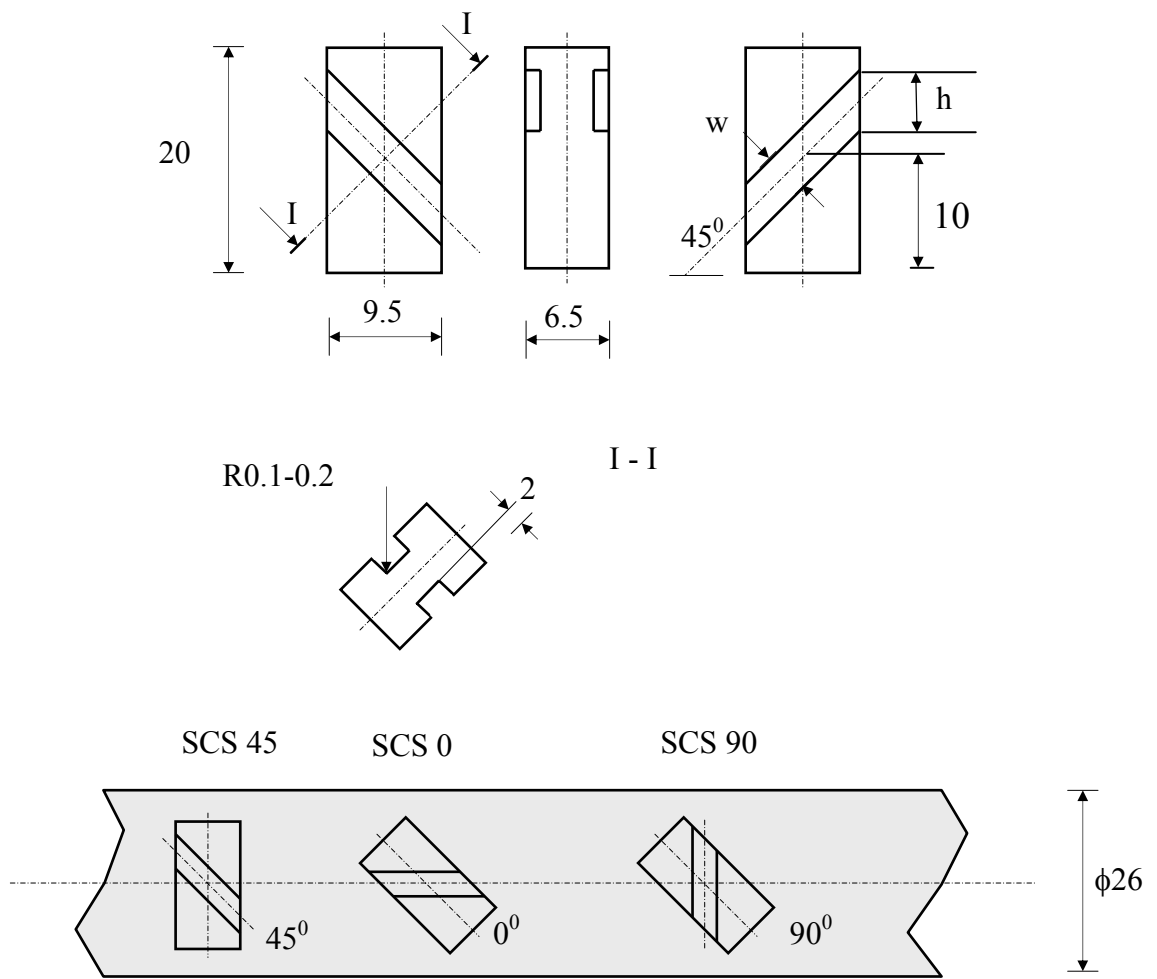


FIGURE 1C

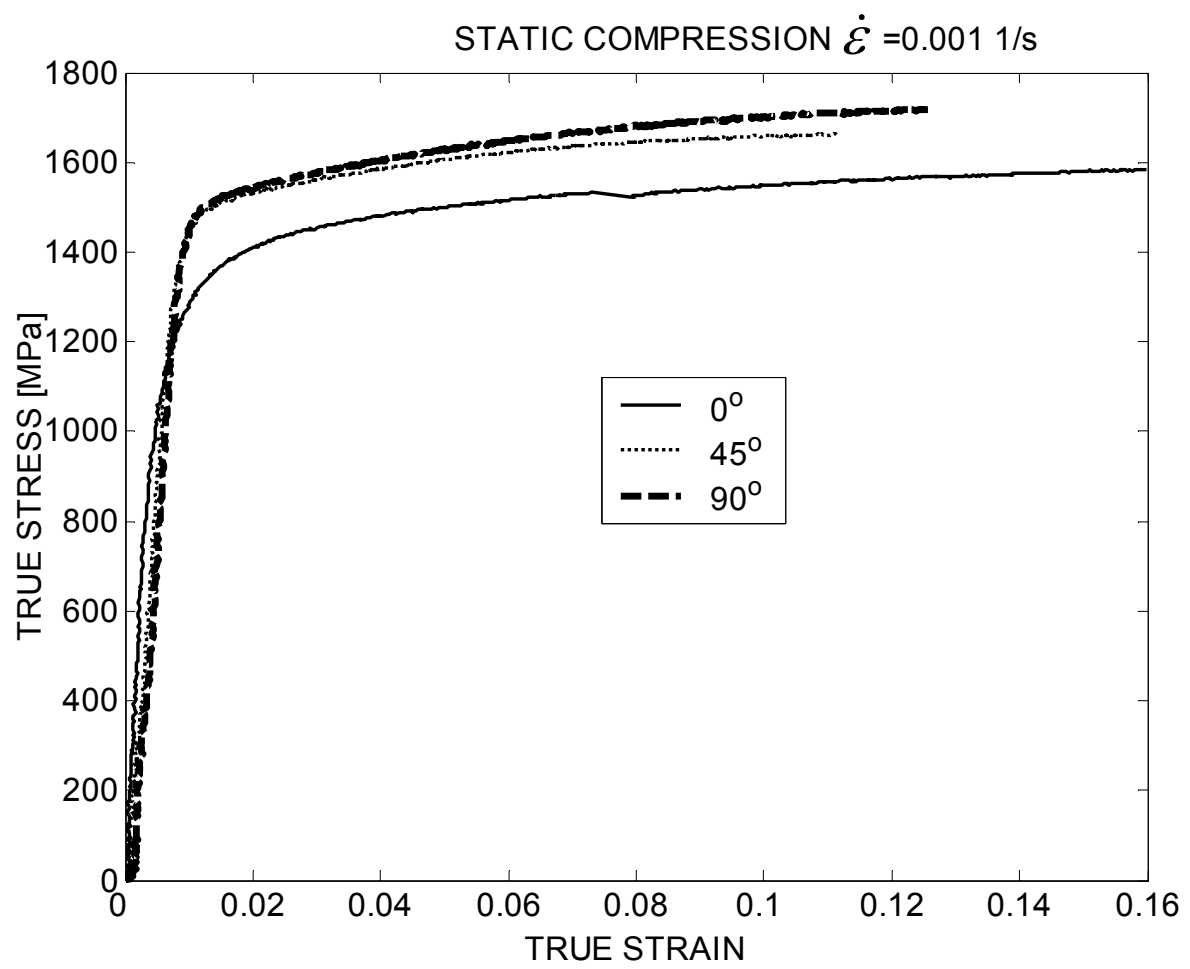


FIGURE 2

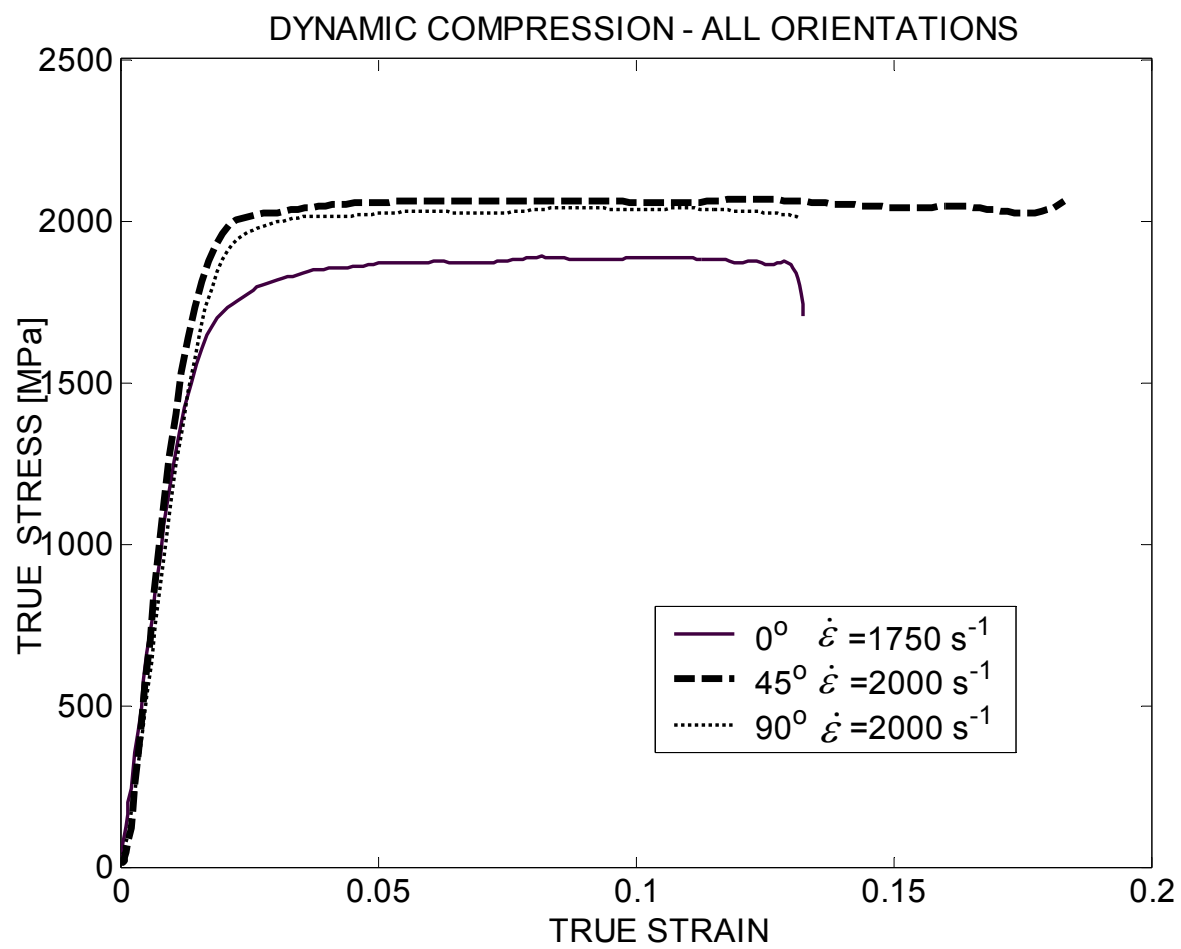


FIGURE 3

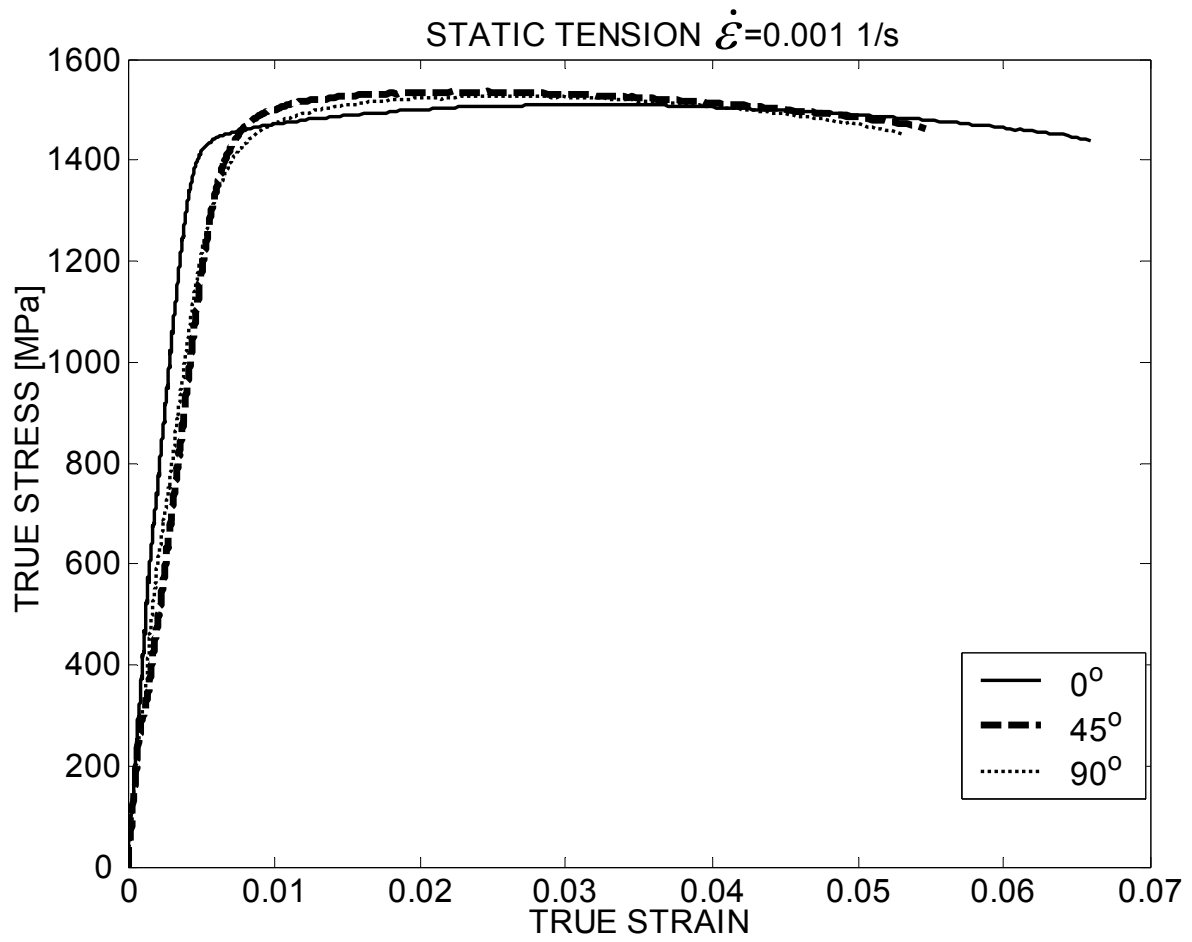


FIGURE 4

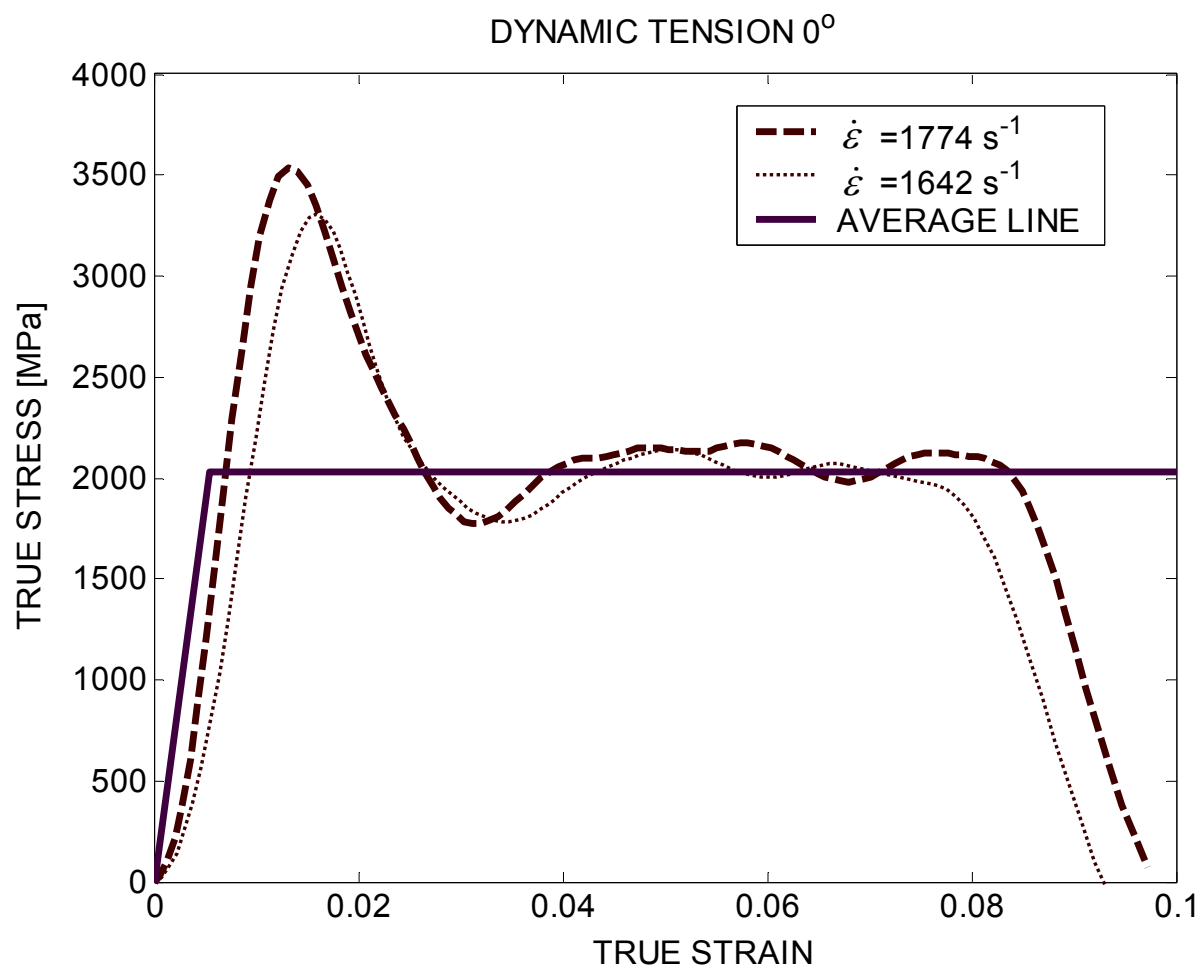


FIGURE 5A

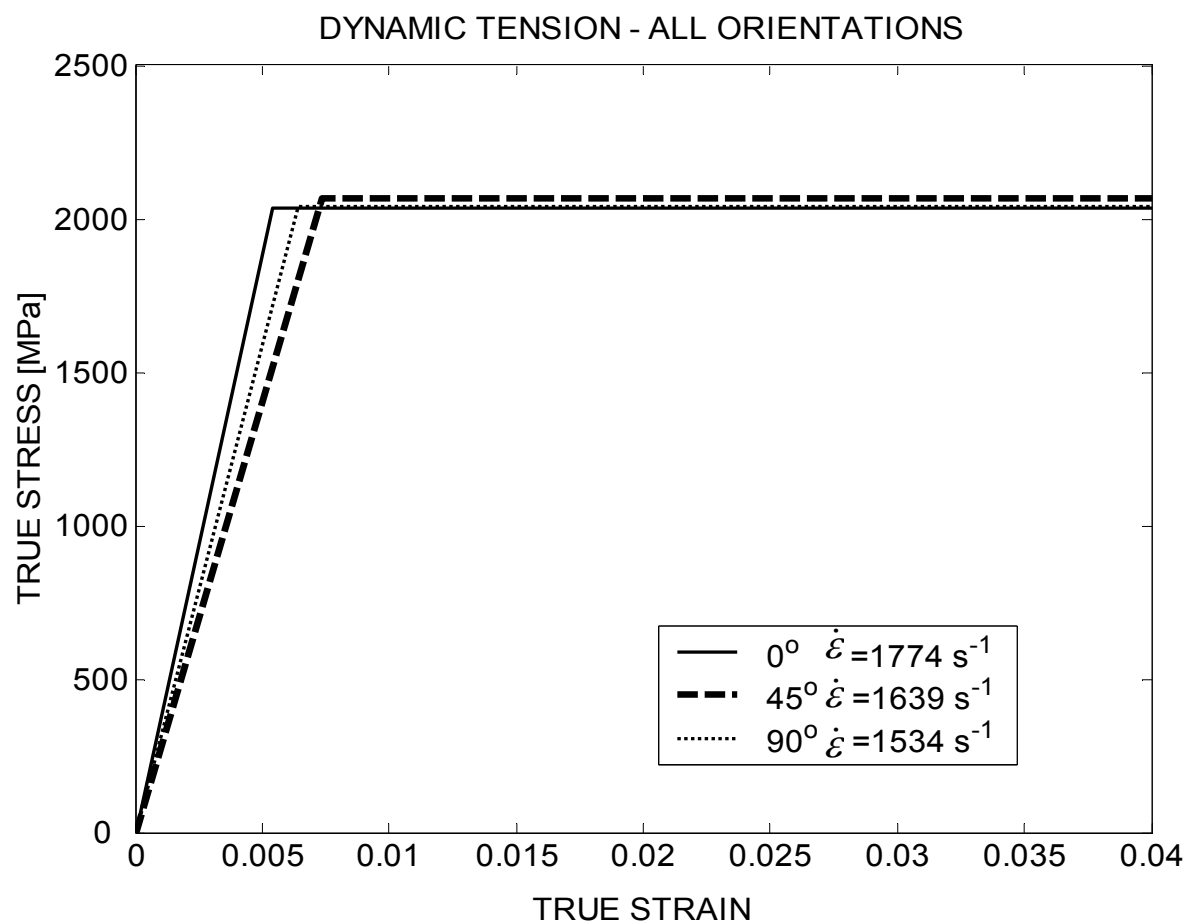
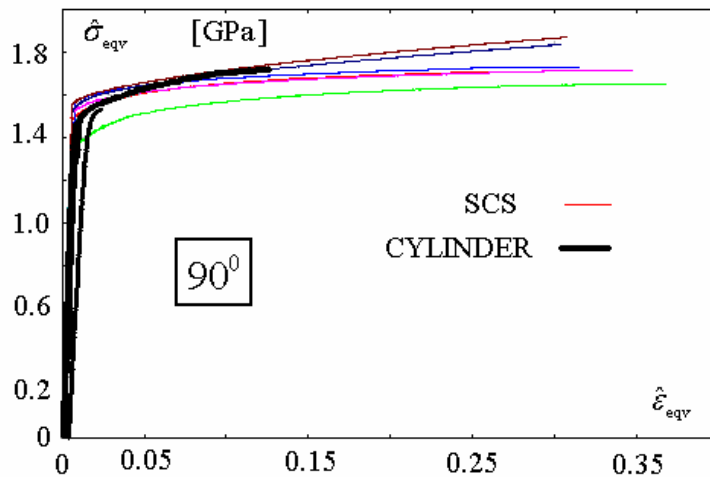
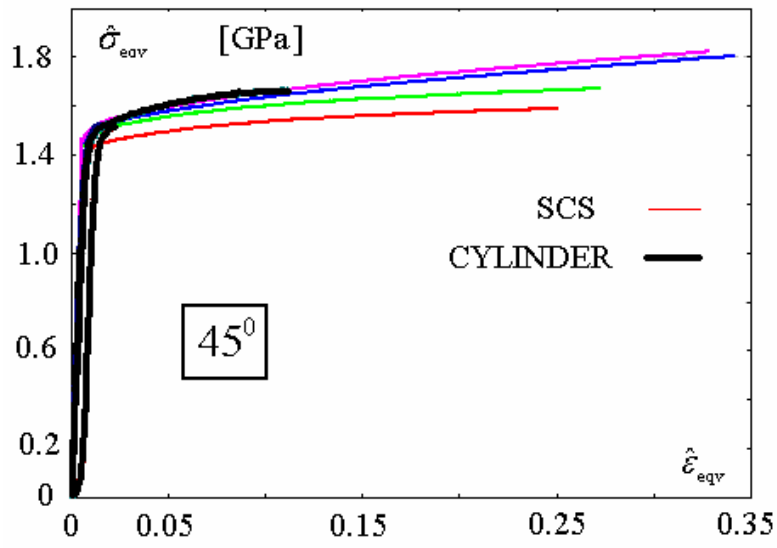
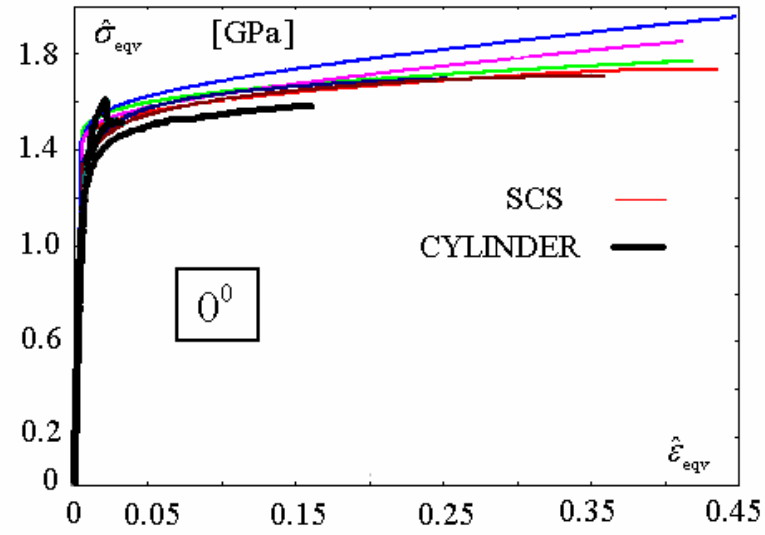


FIGURE 5B



↘

FIGURE 6

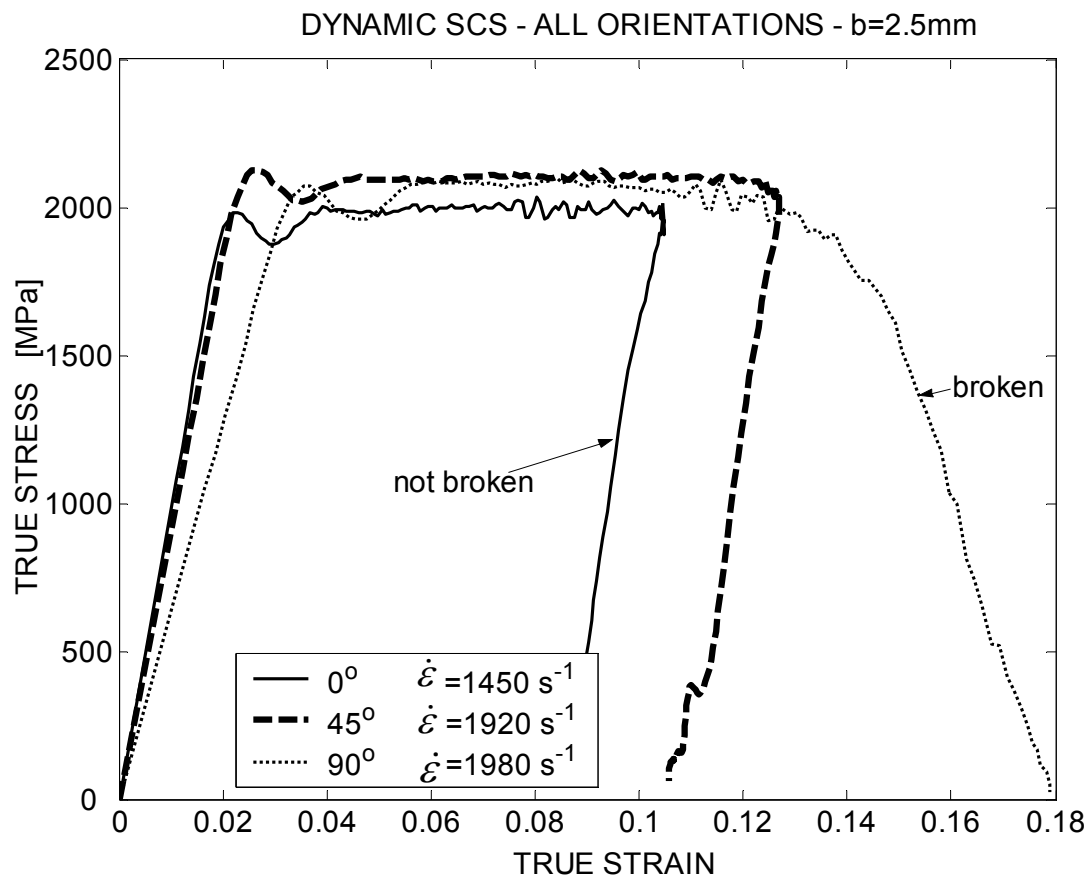


FIGURE 7

FIGURE 8a
Static Tension 0°

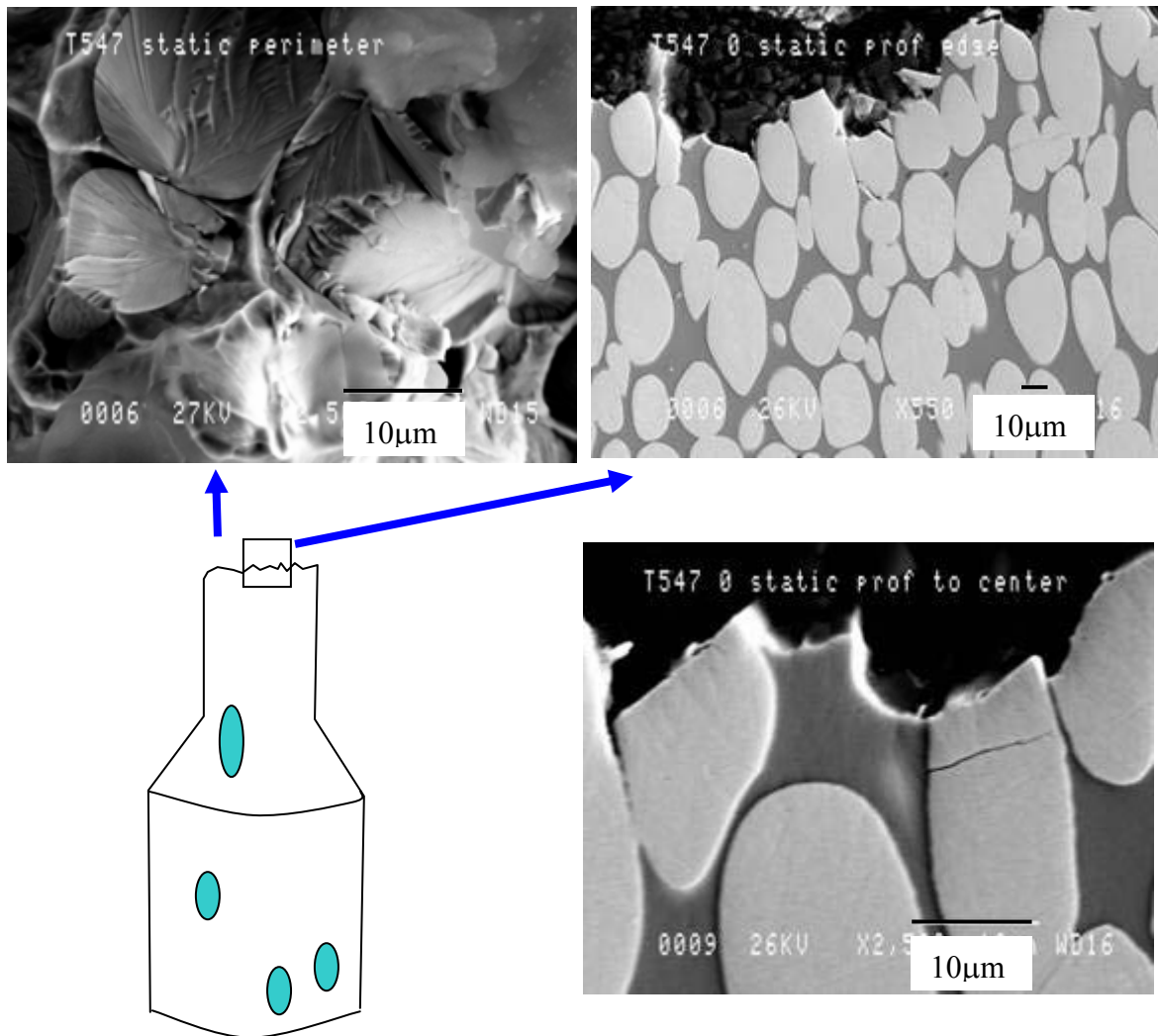


FIGURE 8b

Static Tension 45°

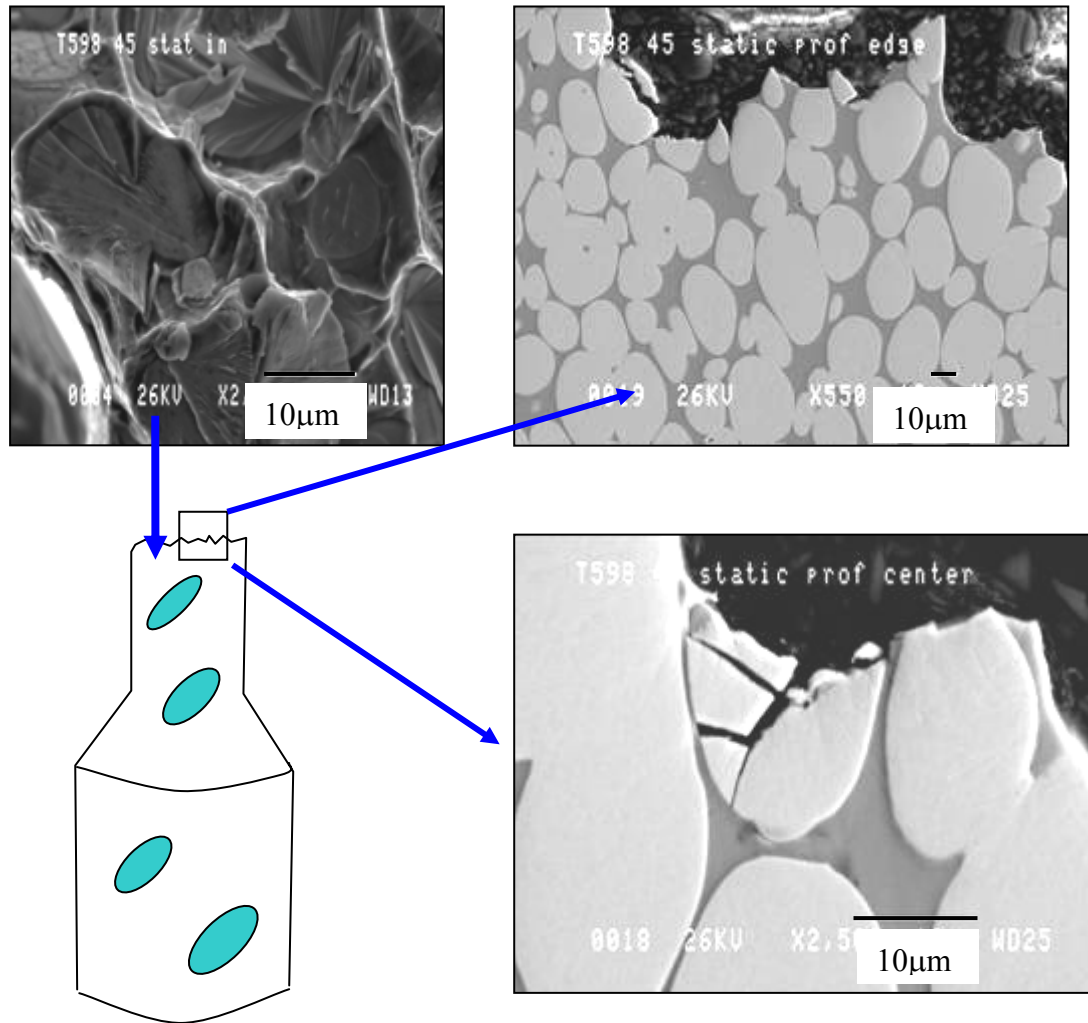


FIGURE 8c

Static Tension 90°

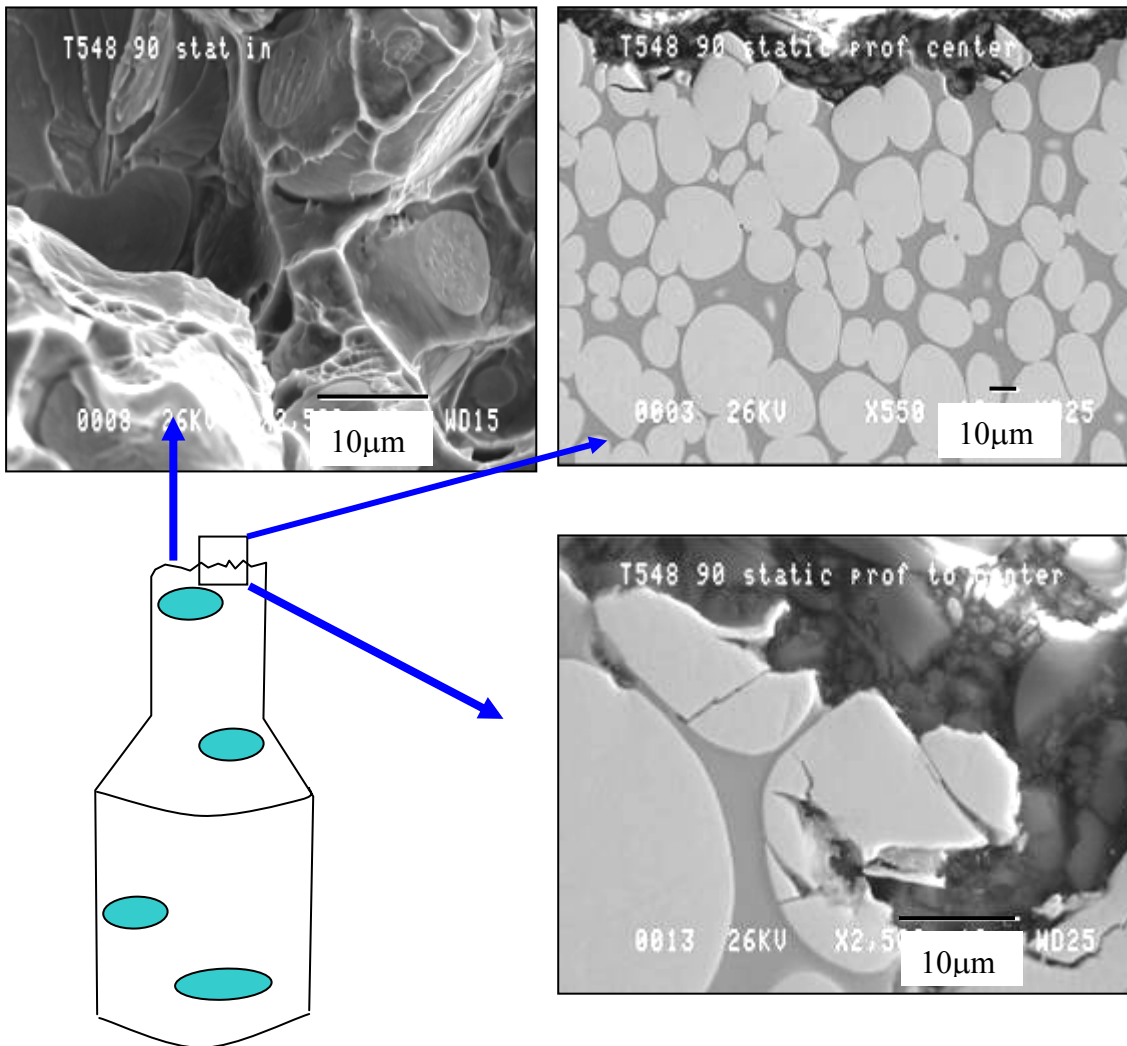




FIGURE 9a
Dynamic Tension 0°

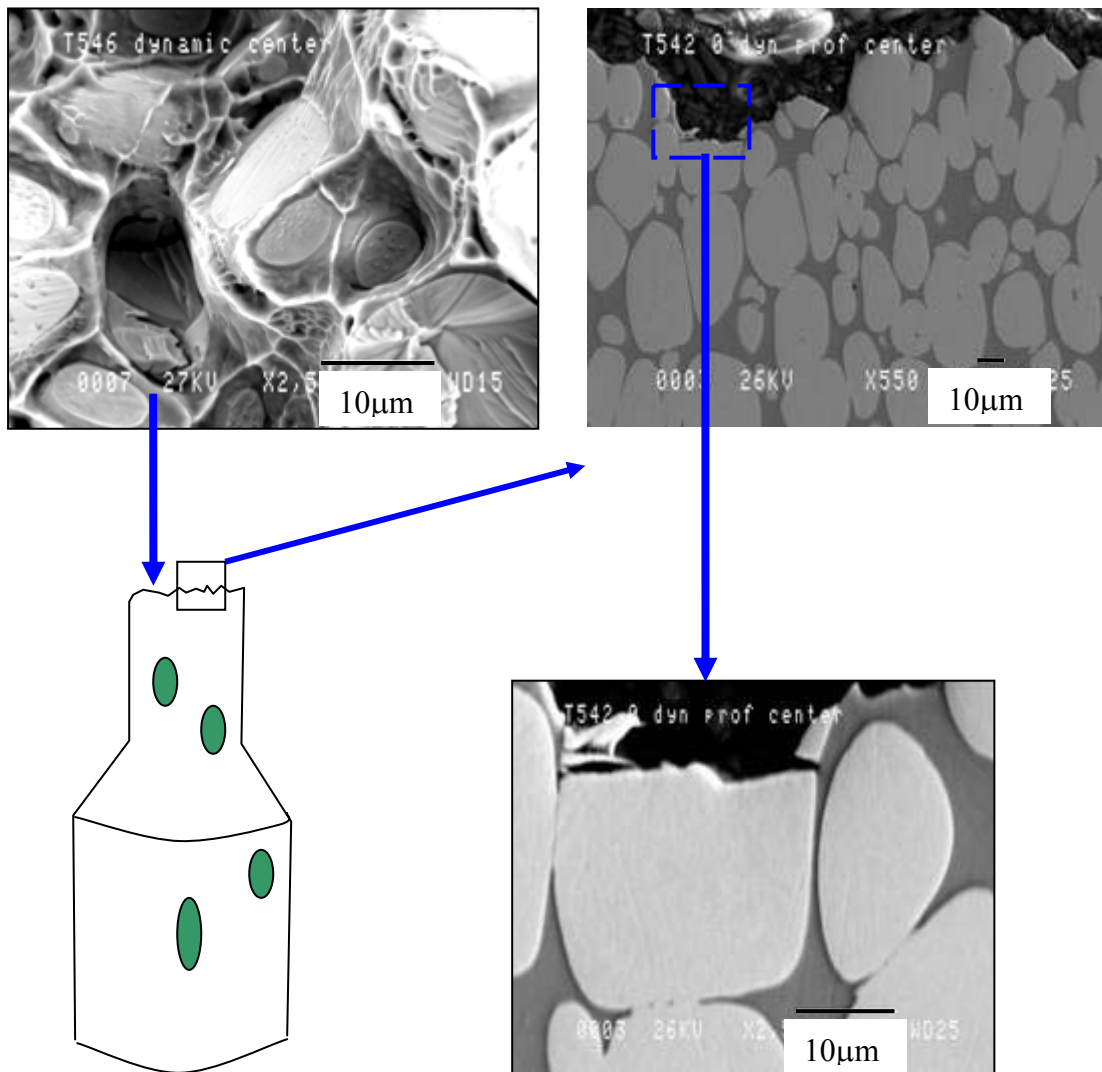


FIGURE 9b

Dynamic Tension 45 °

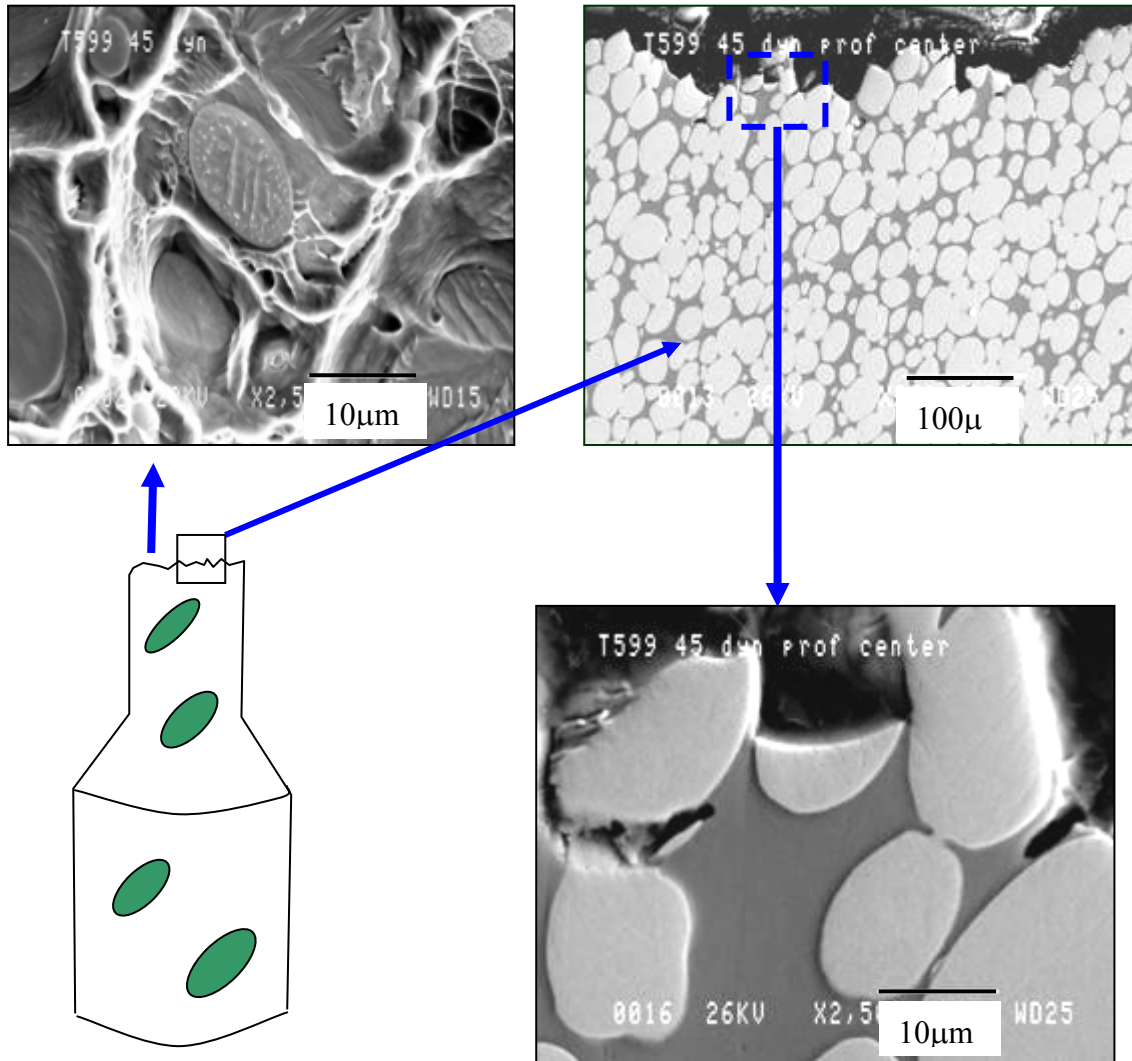


FIGURE 9c
Dynamic Tension 90 °

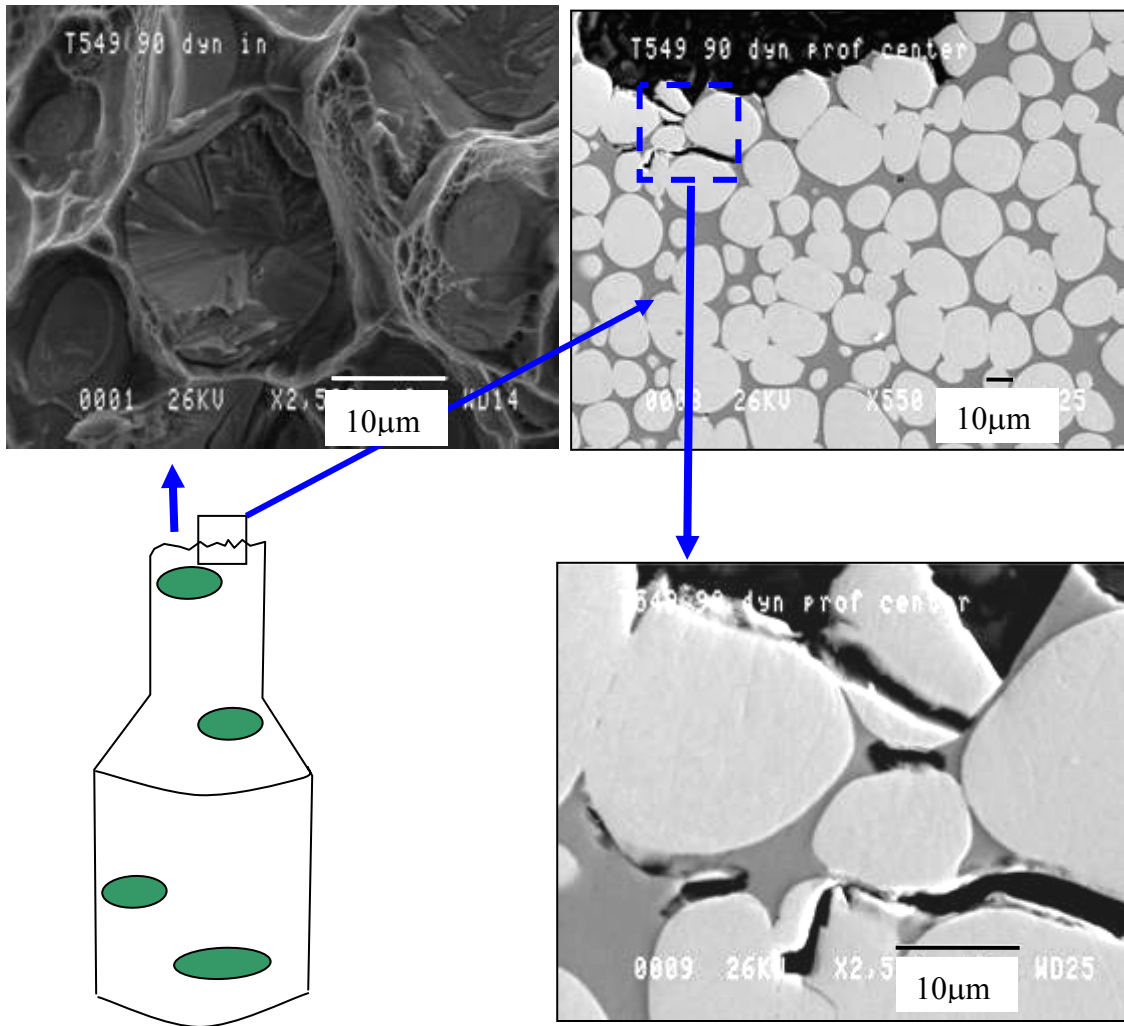


FIGURE 10a

**Static SCS Compression
Gauge Width 2.5mm, 0°**

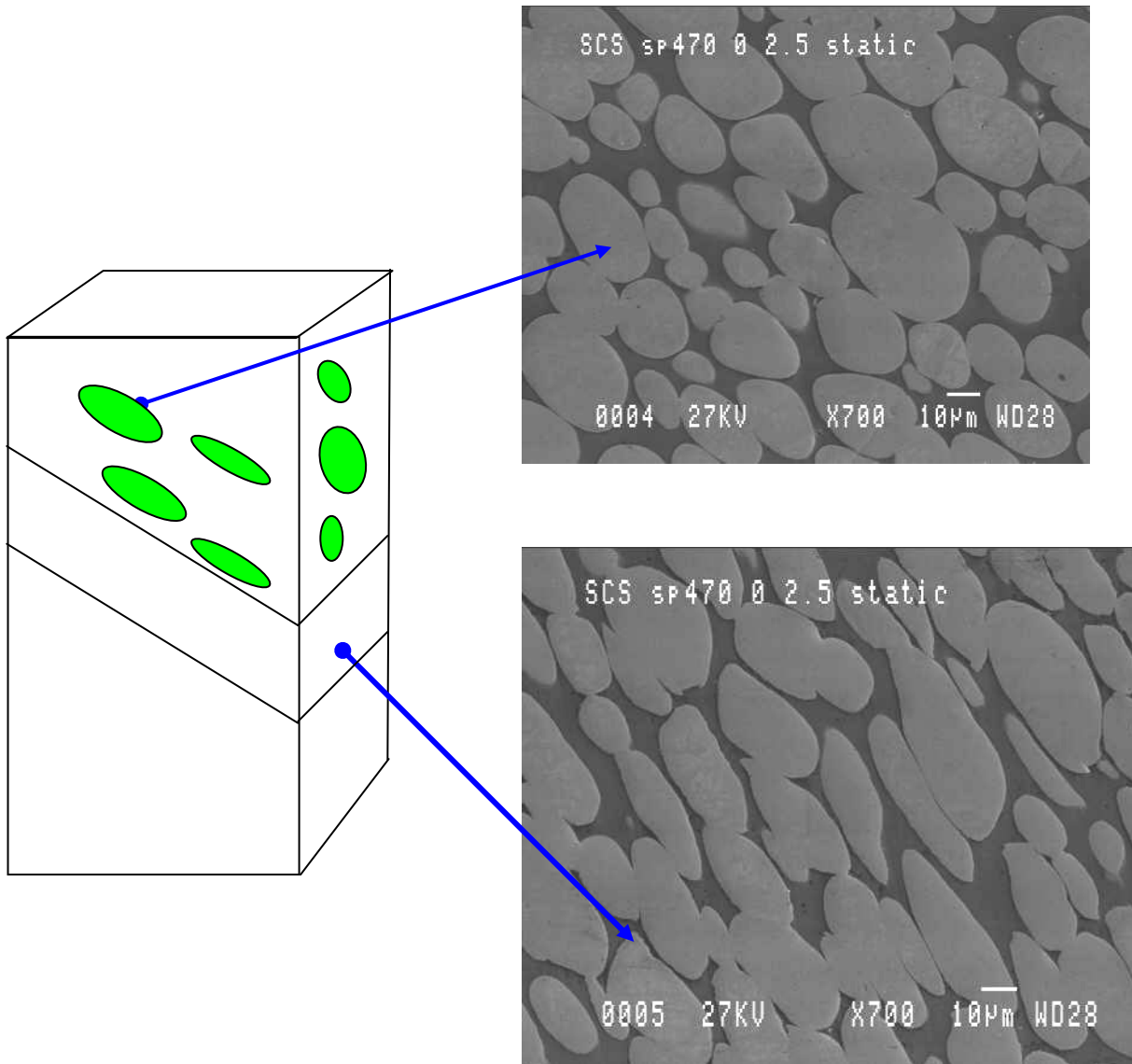


FIGURE 10b

**Static SCS Compression
Gauge Width 2.5mm, 45°**

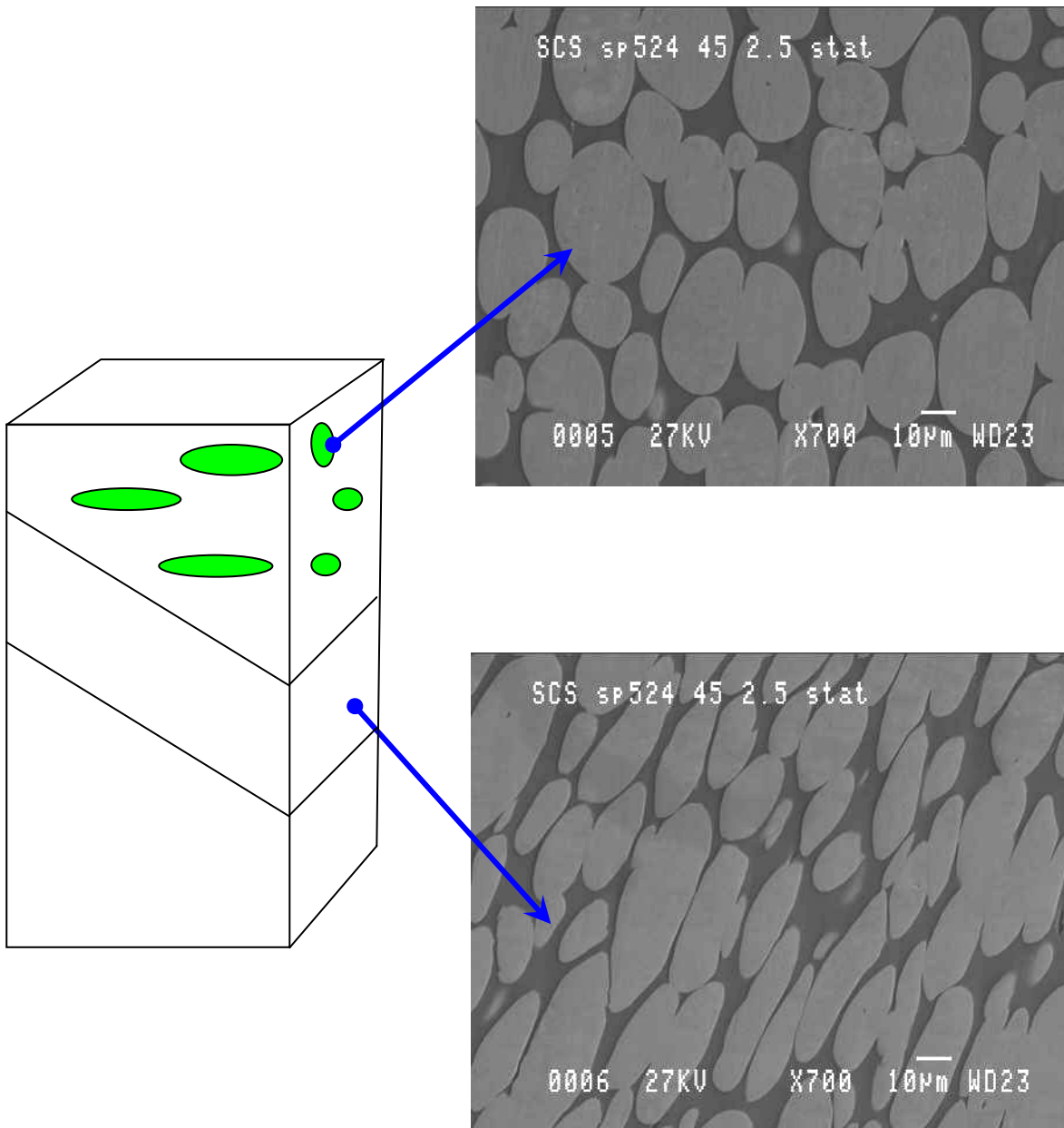


FIGURE 10c

**Static SCS Compression Sp 496
Gauge Width 2.5mm, 90°**

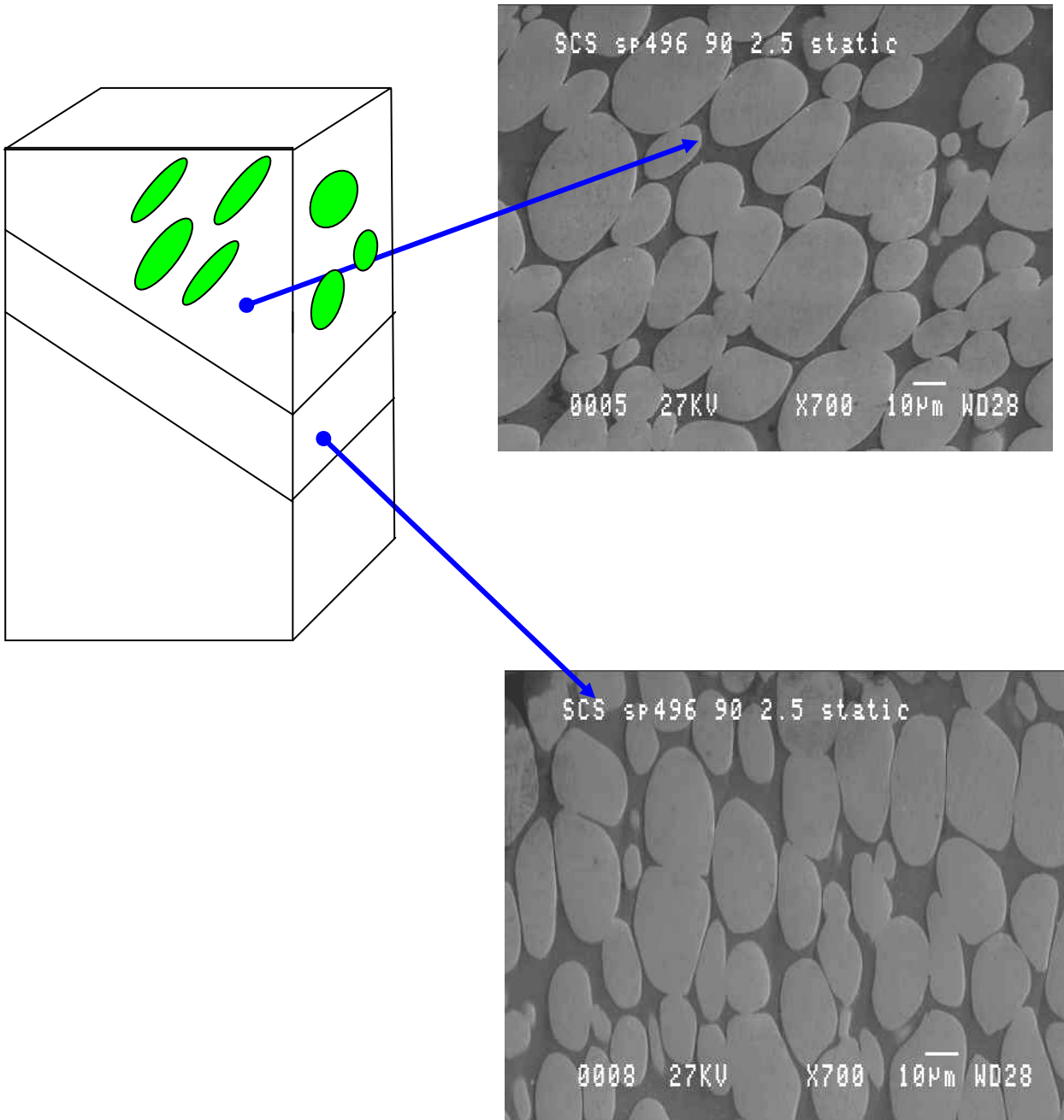


FIGURE 11a

**Dynamic SCS Compression
Gage Width 1 mm, 0°**

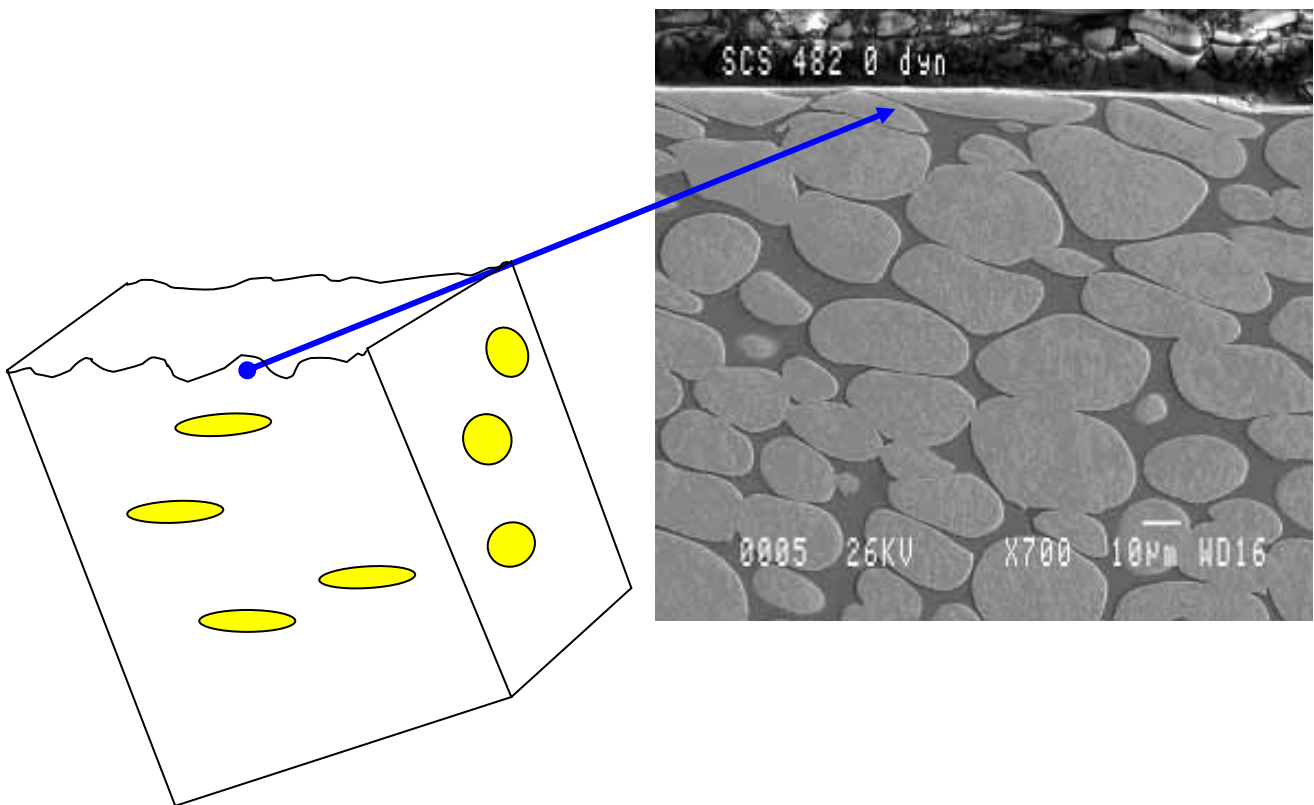


FIGURE 11b

**Dynamic SCS Compression
Gage Width 1 mm, 45°**

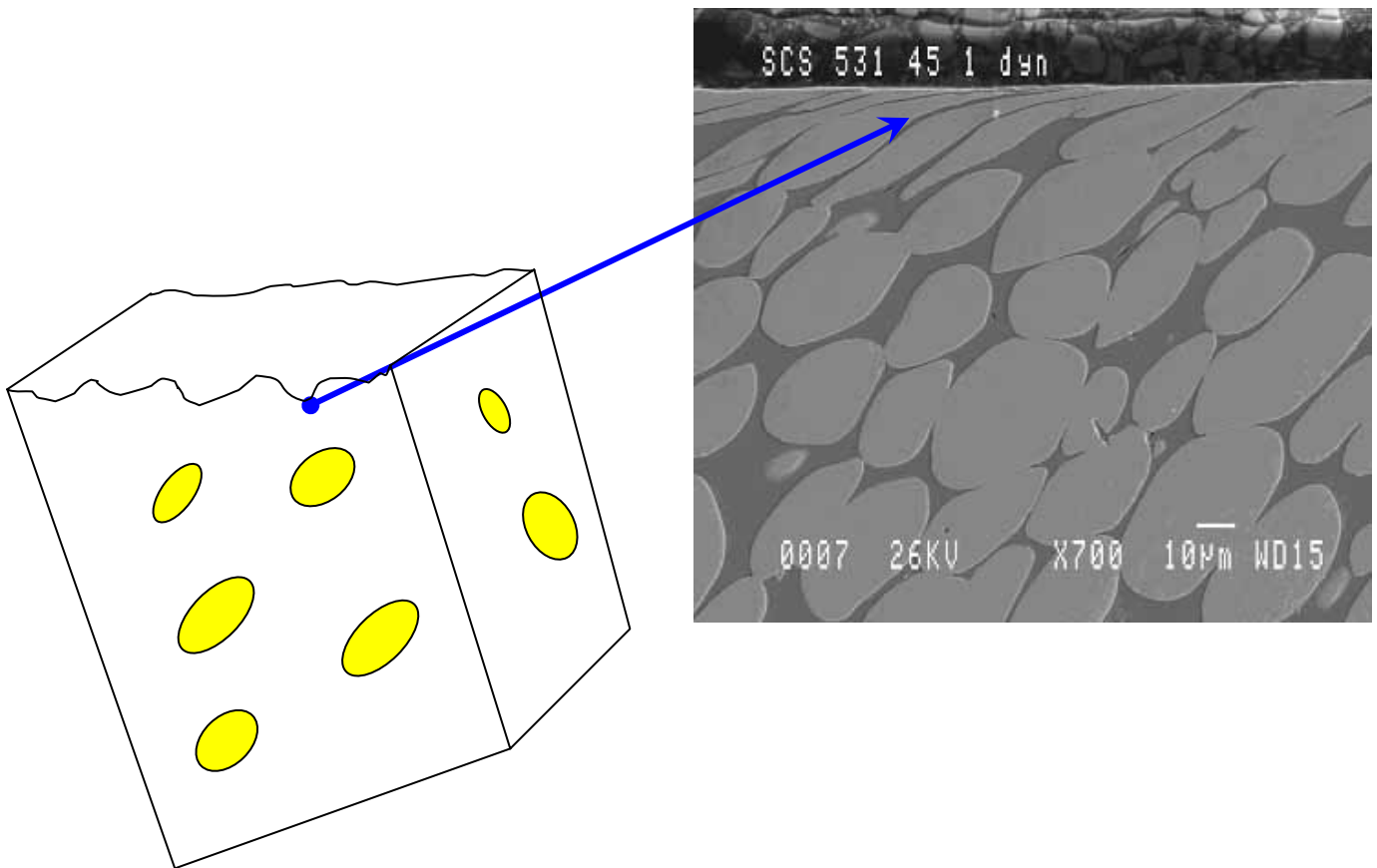


FIGURE 11c

**Dynamic SCS Compression
Gage Width 0.25 mm, 90°**

